ACS OMEGA

Article

Cite This: ACS Omega 2018, 3, 7888−7896

Noninvasive Brain Tumor Imaging Using Red Emissive Carbonized Polymer Dots across the Blood−Brain Barrier

Yang Liu,[†] Junjun Liu,[‡] Jiayi Zhang,[†] Xiucun Li,[†] Fangsiyu Lin,[†] Nan Zhou,*[,§] Bai Yang,*[,‡] and Laijin Lu*[,†]

[†]Department of Hand Surgery, The First Hospital of Jilin University, Changchun, Jilin 130021, China

[‡]State Key Laboratory of Supramolecular Structure and Materials, College of Chemistry, Jilin University, Changchun, Jilin 130012, China

[§]Department of Orthopedics, First Affiliated Hospital of Zhengzhou University, Zhengzhou, Henan 450000, China

Supporting Information

ABSTRACT: Surgical resection is recognized as a mainstay in the therapy of malignant brain tumors. In clinical practice, however, surgeons face great challenges in identifying the tumor boundaries due to the infiltrating and heterogeneous nature of neoplastic tissues. Contrast-enhanced magnetic resonance imaging (MRI) is extensively used for defining the brain tumor in clinic. Disappointingly, the commercially available (MR) contrast agents show the transient circulation lifetime and poor blood−brain barrier (BBB) permeability, which seriously hamper their abilities in tumor visualization. In this work, red fluorescent carbonized polymer dots (CPDs) were systematically investigated with respect to their BBB-penetration ability. In summary, CPDs possess long excitation/emission wavelengths, low toxicity, high photostability, and excellent biocompatibility. CPDs exhibit high internalization in glioma cells in time- and dose-dependent procedures, and internalized CPDs locate mainly in endolysosomal structures. In vitro and in vivo studies confirmed the BBB permeability of CPDs, contributing to the early stage diagnosis of brain disorders and the noninvasive visualization of the brain tumor without compromised BBB. Furthermore, owing to the high tumor to normal tissue ratio of CPDs under ex vivo conditions, our nanoprobe holds the promise to guide brain-tumor resection by real-time fluorescence imaging during surgery.

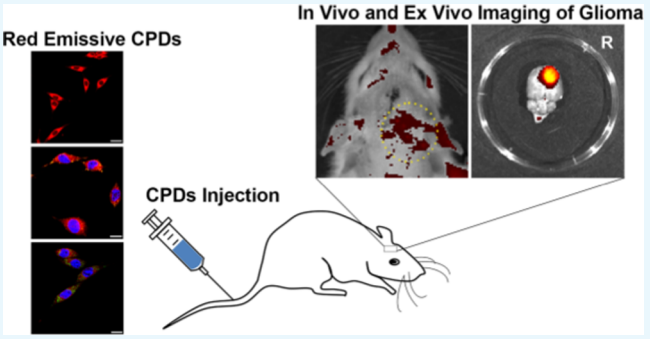

1. INTRODUCTION

Despite the important advances in the diagnosis and treatment of neoplasms, malignant brain tumors still cause the extremely high morbidity and mortality.[1] Currently, surgical resection is recognized as a mainstay in the therapy of malignant brain tumors.[2] However, it is very difficult for surgeons to intraoperatively distinguish the tumor boundaries due to the infiltrating and heterogeneous nature of neoplastic tissues, frequently leading to incomplete surgical resections.[3] The residual neoplastic foci has been associated with the local recurrence and poor prognosis.[4] Conversely, aggressive excision may damage the adjacent crucial areas that control language or movement.[5] Therefore, intraoperative delineation of brain-tumor boundaries is vital for improving the surgical prognosis.

Magnetic resonance imaging (MRI) is a powerful neuro-imaging technique for preoperative detection and localization of brain tumor.[6] Gadolinium (Gd) chelates as MR contrast agents (CAs) are widely used to delineate tumor margins in clinic.[7] These CAs could lead to MR signal enhancement in tumor areas, where the blood−brain barrier (BBB) is disrupted. Unfortunately, early brain disorders and many malignant brain tumors cannot be enhanced because of the uncompromised BBB.[8,9] Moreover, the tumor boundaries delineated by preoperative MRI are always not completely aligned to the actual margins due to brain shifts during surgery.[10] Even though this problem can be overcome through intraoperative MRI, it usually requires repeated administration of Gd chelates due to their transient circulation lifetime, which may result in inaccuracies caused by false-positive contrast enhancement.[11] Furthermore, the high running costs and time-consuming procedures of intraoperative MRI also limit its applications during surgery.[12] Therefore, the ideal probes for brain tumor imaging would have the optimized circulation lifetime and the capability to cross intact BBB.

Recently, optical fluorescent imaging technique has been widely used to improve intraoperative tumor visualization.[13,14] The fluorescent dyes, such as 5-aminolevulinic acid and

Received: May 29, 2018
Accepted: June 11, 2018
Published: July 16, 2018

DOI: 10.1021/acsomega.8b01169
ACS Omega 2018, 3, 7888−7896

fluorescein, can be used as imaging agents to label malignant brain tumors successfully.[13] However, these agents included some limitations, such as false-positive labeling and lack of tumor specificity.[14] Moreover, they require a broken-down BBB to leak into the areas of brain tumors to achieve the tumor labeling.[15] To our knowledge, nanoprobes demonstrate great potential in tumor imaging due to their tunable circulation lifetime, imaging sensitivity and targeting specificity, and enhanced permeability and retention (EPR) effect that increase the intratumoral delivery.[16] Even though previous studies exhibit the ability of nanoprobes to visualize extracranial tumor xenografts in vivo,[17,18] the application of nanoprobes in brain tumor imaging is barely satisfactory because the BBB prevents almost all exogenous macromolecules from entering the brain.[19] Therefore, the BBB is regarded as a big challenge for the intracerebral delivery of nanoprobes, which seriously hinders the diagnosis and therapy of brain diseases. Quantum dots are attractive nanoparticles (NPs) and possess excellent optical properties. Though they can provide real-time imaging during the brain tumor resection, they are limited to their potential toxicities.[15] Recently, photoluminescent carbon dots (CDs) have attracted increasing interest because of their superior optical properties, low toxicity, high photostability, excellent biocompatibility, and easy modifications.[20,21] Moreover, compared to traditional organic dyes and semiconductor quantum dots, CDs are regarded as promising fluorescent probes in biomedical applications, such as bioimaging and biosensing.[22−24] Therefore, it is of high importance to develop carbon-based nanoparticles that can cross the BBB and realize the brain tumor imaging.

In our recent studies, *o*-phenylenediamine (*o*PD) and HNO_3 have been used to synthesize red emissive carbonized polymer dots (CPDs), which show the optimal emission at around 630 nm and extremely high quantum yield (QY) around 10.83% (in water) and 31.54% (in ethanol).[25] The red emissive CPDs could be used for in vivo imaging due to the strong tissue penetration capability of their fluorescence. To our knowledge, the transport of CPDs across the BBB has not previously been researched systematically. Herein, our goal is to comprehensively evaluate the BBB permeability of CPDs and their potential application for brain tumor imaging. First, we study the cellular behaviors of CPDs in C6 brain glioma cells. Subsequently, we evaluate the BBB-penetration capability of CPDs in vitro and in vivo. Finally, C6 glioma-bearing rats are used to investigate the targeting effect of CPDs. In summary, in vitro and in vivo studies confirm the BBB permeability of CPDs, contributing to the early stage diagnosis of brain disorders and the noninvasive visualization of the brain tumor without compromised BBB. In addition, CPDs could successfully distribute into the orthotopic brain glioma with high tumor to normal tissue ratio, demonstrating the feasibility to guide brain-tumor resection by real-time fluorescence imaging during surgery.

2. RESULTS AND DISCUSSION

2.1. Preparation and Characterization of CPDs. We previously reported the preparation of excitation-independent red emissive CPDs through one-step hydrothermal method using *o*-phenylenediamine (*o*PD) and HNO_3, and they exhibited narrow bandwidth emission and extremely high QY around 10.83% (in water) and 31.54% (in ethanol). Furthermore, they exhibited an excitation-independent photoluminescence with the optimal emission at around 630 nm and a shoulder peak at 677 nm. The UV−vis absorption spectrum of CPDs showed several absorption bands at 282 and 535−621 nm. Transmission electron microscopy (TEM) image of CPDs indicated that CPDs were nearly spherical with uniform size (ca. 5.74 nm). The ζ-potential of CPDs was ca. +1.5 mV. We have described the detailed characterization of CPDs in our previous work.[25]

2.2. Cytotoxicity of CPDs in Glioma Cells. Low cytotoxicity is a prerequisite for CPDs to be applied in the biological field. To investigate the cytotoxicity of CPDs, an 3-(4,5-dimethylthiazol-2-yl)-2,5-diphenyltetrazolium bromide (MTT) assay was conducted on the C6 glioma cells. After 24 h incubation with a series of concentrations of CPDs (50−400 μg mL^{-1}), the cell viability of C6 remained above 80% at concentrations as high as 400 μg mL^{-1} (Figure 1). Thus, it was

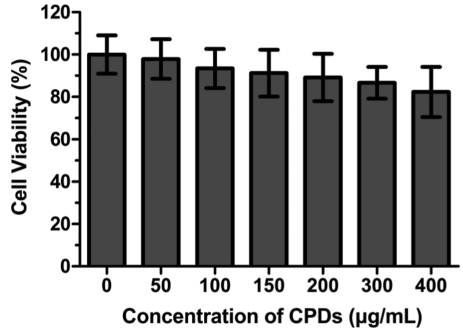

Figure 1. Low cytotoxicity of CPDs in C6 brain glioma cells. The values are represented as mean ± standard deviation (SD) (n = 6).

concluded that CPDs displayed low toxicity, which was similar with our previous studies.[25,26] Compared with semiconductor quantum dots, this fascinating advantage gives CPDs a great potential to be a promising bioprobe in the future clinical applications.[27,28]

2.3. Physiological Stability of CPDs. The surface charge and size were investigated to evaluate the physiological stability of CPDs after 2 h incubation with C6 cells. We found the ζ-potential of CPDs did not significantly change after 2 h incubation with C6 cells, indicating the good stability of surface state of CPDs. Some medium electron dense particles within an endocytic vesicle of the cytoplasm were observed using transmission electron microscopy (TEM, Figure S1B). Moreover, high-resolution TEM image (Figure S1C) showed that the size of these particles was similar with CPDs,[25] which further confirmed the excellent physiological stability of CPDs after entering the cells.

2.4. Cellular Uptake of CPDs. To understand the cellular behaviors of CPDs on C6 glioma cells, the cellular uptake kinetics of CPDs should be elucidated first. The cells were exposed to 200 μg mL^{-1} CPDs for a series of time periods (5−120 min), and the fluorescence intensity of cells was then detected using confocal laser scanning microscopy (CLSM) to evaluate the uptake amount of CPDs. As shown in Figure 2A, after 5 min incubation, the CPDs could enter the cells and yield bright red fluorescence, suggesting their great potential for glioma imaging.[14,29] Moreover, the enhanced fluorescence intensity of cells was observed over time and CPDs showed a strong red fluorescence at 120 min incubation. CPDs also exhibited highly efficient internalization in human umbilical vein endothelial cells (HUVEC), which could be used to

DOI: 10.1021/acsomega.8b01169
ACS Omega 2018, 3, 7888−7896

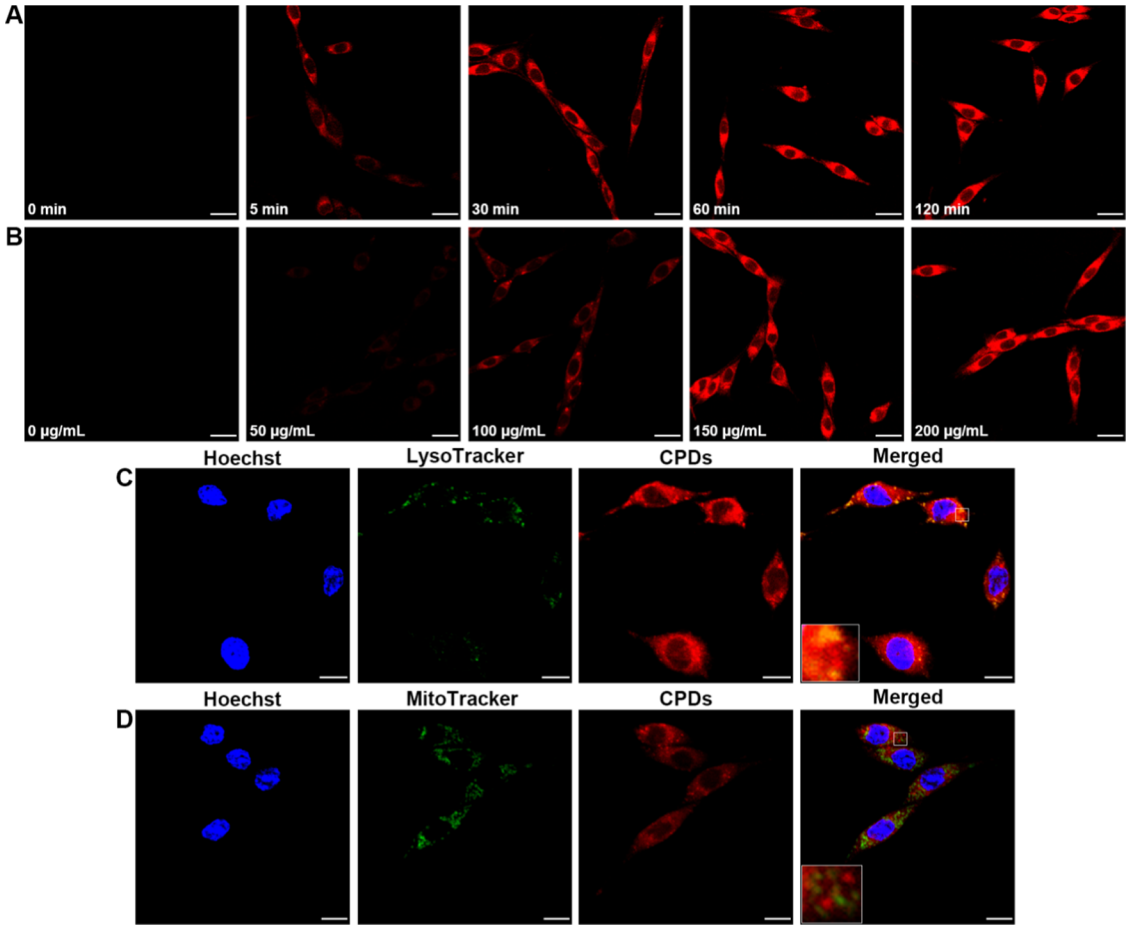

Figure 2. CLSM images of the cellular behaviors of CPDs in C6 cells. (A) C6 cellular uptake of CPDs for different times; (B) C6 cellular uptake of CPDs at different concentrations; the scale bar represents 20 μm. (C, D) Subcellular localization of CPDs in C6 cells was investigated using organelle-specific probes: Hoechst 33342 (a blue nuclear dye), LysoTracker Green DND-26, and MitoTracker Green were used to localize the nucleus, lysosomes, and mitochondria, respectively; the yellow fluorescence in the merged image showed the colocalization of CPDs and lysosomes; the scale bar represents 10 μm. The representative areas are magnified optically.

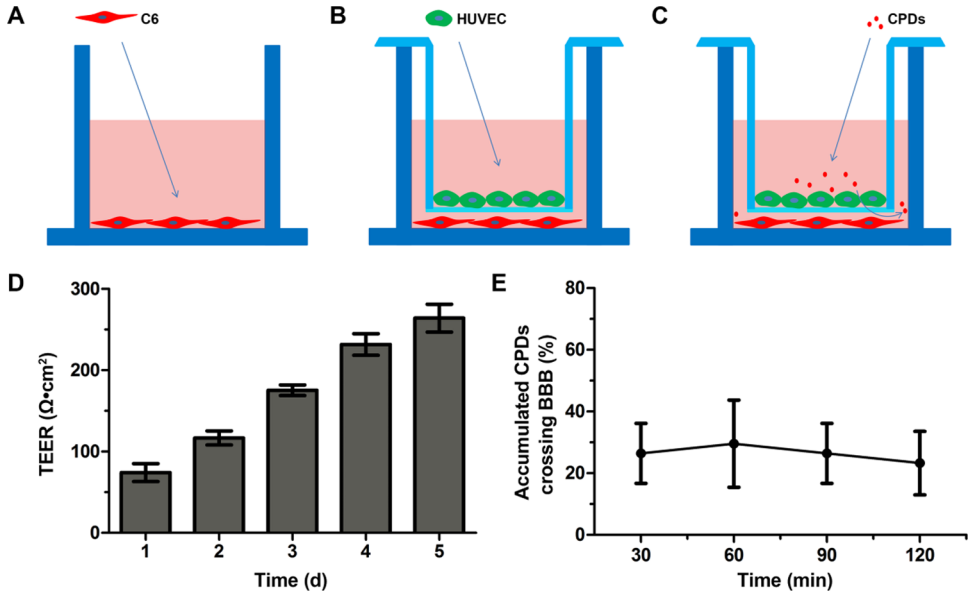

Figure 3. Evaluation of the BBB-penetration ability of CPDs in vitro. (A–C) Schematic diagram of the preparation and application of the in vitro BBB model: (A) the 12-well plates were seeded with C6 cells; (B) HUVEC were seeded into the transwell inserts; (C) CPDs were added into the transwell lumen, and the fluid in the lower compartment containing the CPDs could be detected. (D) Time-dependent TEER values of the in vitro BBB model (n = 3, mean ± SD). (E) Accumulated percentages of CPDs that crossed the BBB (n = 6, mean ± SD).

DOI: 10.1021/acsomega.8b01169
ACS Omega 2018, 3, 7888–7896

establish an in vitro BBB model (Figure S2). Subsequently, C6 cells were exposed to CPDs at different concentrations (50–200 μg mL^{-1}) for 1 h. The cellular uptake of CPDs would also enhance when increasing the concentration of CPDs (Figure 2B). These results suggested that the internalization of CPDs into C6 cells involved in time- and dose-dependent procedures was consistent with the behaviors of other nanoparticles.[30−33]

2.5. Subcellular Location of CPDs. We further evaluated the intracellular localization of CPDs in C6 cells using costaining methods with two organelle-specific probes, including LysoTracker Green DND-26 and MitoTracker Green. As shown in Figure 2C, the yellow fluorescence could be observed in the merged image, which demonstrated that internalized CPDs mainly distributed in lysosomes. However, CPDs could not be transported to the mitochondria because there was no significant colocalization of CPDs with MitoTracker Green in Figure 2D. Moreover, the Pearson correlation coefficient (R_r) was calculated to confirm these results. R_r for LysoTracker Green DND-26 was 0.57, suggesting the good colocalization between CPDs and lysosomes. However, R_r for MitoTracker Green was −1, indicating no colocalization between CPDs and MitoTracker Green. Therefore, we inferred that endolysosomal structures mediated the internalization of CPDs in C6 cells, which was the most common manner for cells to take up nanoparticles (NPs).[34,35]

In general, different characteristics of NPs would influence their cellular internalization and distribution, which were directly associated with their biosafety and potential biomedical applications.[36−38] Our study indicated that the internalized CPDs located mainly within lysosomes but not significantly entered the mitochondria. We speculated that the nanometer size and surface ζ-potential of CPDs played a critical role in their internalization and distribution in C6 cells.[39−41] In addition, CPDs could serve as nanocarriers for drug delivery due to their subcellular distribution.[42,43] No obvious entrance of CPDs to the mitochondria might explain their low cytotoxicity owing to the negligible interference to the mitochondrial respiratory chain.[26,44]

2.6. BBB-Penetration Ability of CPDs in Vitro. To evaluate the BBB-penetration capability of CPDs in vitro, human umbilical vein endothelial cells (HUVEC) and C6 brain glioma cells were used to establish an in vitro BBB model. The process of constructing an in vitro BBB model is displayed using a schematic diagram in Figure 3A−C. This BBB model was very close to the in vivo BBB in morphology and function.[45,46] As shown in Figure 3D, the transendothelial electrical resistance (TEER) was measured to assess and monitor the integrity of the in vitro BBB every day. The high TEER values obtained suggested that the coculture BBB model could be successfully established to mimic the microenvironment of in vivo BBB.[47,48] Before investigating the BBB-penetration capability of CPDs, an MTT assay was conducted to evaluate the cytotoxicity of CPDs at a concentration of 2 mg mL^{-1} on HUVEC and C6 cells. After 2 h incubation with CPDs (2 mg mL^{-1}), the cell viability of HUVEC and C6 cells remained above 90%, indicating that 2 mg mL^{-1} of CPDs could not significantly damage the integrity of the BBB model (Figure 4).

The BBB-penetration capability of the CPDs was evaluated via detecting the florescence intensity of the BBB-penetrating CPDs, which accumulated in the lower compartment of a BBB model (Figure 3C). As shown in Figure 3E, the percentage of

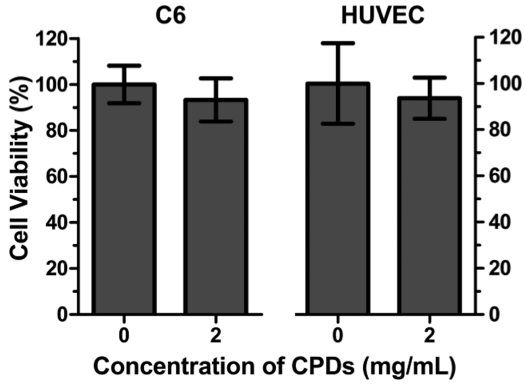

Figure 4. Viability of C6 cells and HUVEC after incubation with 2 mg mL^{-1} of CPDs for 2 h (n = 6, mean ± SD).

BBB-penetrating CPDs reached the highest after 60 min incubation and could maintain 20−40% within 120 min incubation, suggesting the excellent BBB-penetration capability of the CPDs. The BBB could prohibit the effective delivery of therapeutics from circulating blood to the central nervous system, which was mainly attributed to the tight junctions of endothelial cells.[49,50] However, the intercellular tight junctions have 4−6 nm gaps in the blood−brain barrier.[51] Therefore, we inferred that the CPDs could cross the BBB through such gaps because the size of CPDs was around 5.74 nm. In addition, the cationic surface charge on CPDs also increased the permeability of BBB by charge neutralization, leading to an enhanced transcytosis of CPDs through the blood−brain barrier.[52,53] CPDs exhibited highly efficient internalization in HUVEC and C6 cells according to our previous studies, so we speculated that the actual percentages of BBB-penetrating CPDs were higher than the measured values. Therefore, CPDs could be used as excellent bioprobes or nanocarriers for the diagnosis and treatment of brain disorders due to their high BBB-penetration ability.[8,54,55]

2.7. BBB-Penetration Ability of CPDs in Vivo. The BBB permeability of CPDs was further demonstrated in vivo using normal Sprague-Dawley rats. The rats were administrated with CPDs (30 mg kg^{-1}, 200 μL) through the tail vein injection. After different time intervals, the brain tissues of rats were harvested and imaged with an in vivo optical imaging system (IVIS Spectrum, Caliper). As shown in Figure 5, we observed

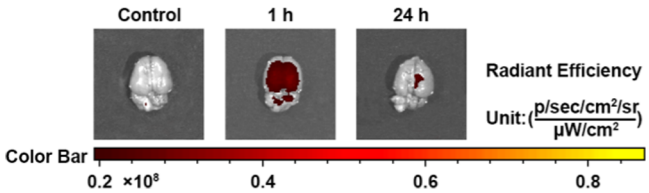

Figure 5. Ex vivo fluorescence images showing the BBB-penetration ability of CPDs in vivo.

the bright red fluorescence signal of CPDs at 1 h postinjection, suggesting that CPDs could penetrate the blood−brain barrier and relatively uniformly distribute within the brain tissue. Moreover, there was still fluorescence signal in the brain at 24 h after injection, indicating that CPDs had long circulation lifetime and could be retained in the brain for a long time. These results implied that CPDs could pass through the BBB in physiological conditions, which was the attractive advantage

DOI: 10.1021/acsomega.8b01169
ACS Omega 2018, 3, 7888−7896

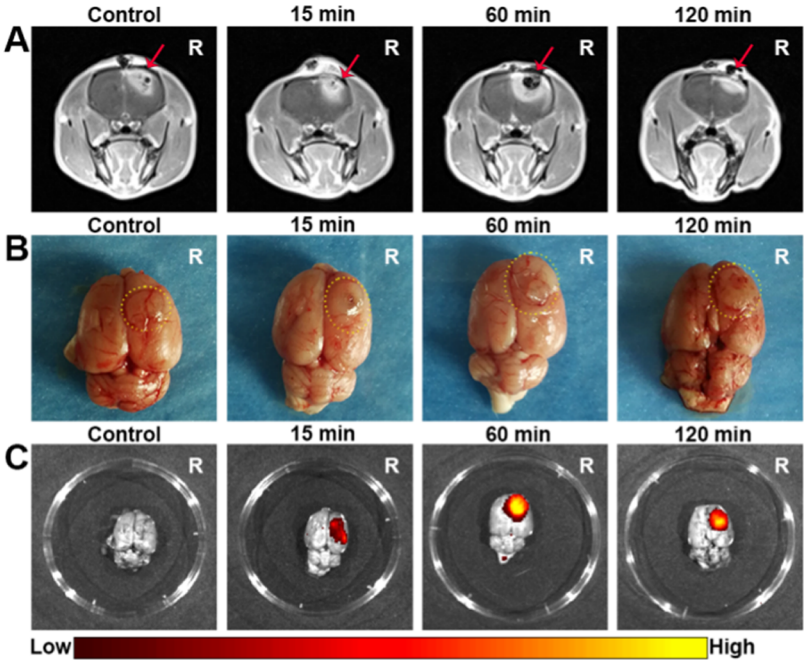

Figure 6. Ex vivo imaging of glioma-bearing rats after tail intravenous injection of CPDs. (A) MRI was used to determine the tumor formation at 13 days after implantation; the red arrows indicated the tumor tissues. (B) Photographs of isolated brains; the dotted circles showed the tumor tissues. (C) Ex vivo fluorescence imaging of brains at selected time points.

for NPs and was first reported for carbon-based nanomaterials to the best of our knowledge.[56−58] Diagnosis of patients with brain tumors at an early time point remains an intractable problem in the clinic. Therefore, CPDs have potential clinical application in early stage diagnosis and treatment of brain disorders, when the blood−brain barrier is not disrupted or loosened.[8,59] In addition, CPDs also have the promise to noninvasively target many malignant brain tumors with uncompromised BBB, such as glioblastoma multiforme and anaplastic astrocytoma.[9]

2.8. In Vivo and ex Vivo Imaging of Orthotopic Glioma-Bearing Rats. The orthotopic glioma models were established to investigate the targeting effect of CPDs. MRI was used to determine the tumor progression at 13 days after implantation, indicating the successful establishment of orthotopic glioma model (Figure 6A). After intravenous injection of CPDs via the tail, in vivo and ex vivo imagings of the brain tissues of C6 glioma-bearing rats were performed using an in vivo optical imaging system. As shown in Figure S3, CPDs could pass through the BBB and target the glioma, suggesting that the long-wavelength emission of CPDs facilitated the in vivo imaging of glioma and avoided autofluorescence from the skull and scalp. In addition, the outline of brain glioma was consistent with that of the ex vivo imaging in Figure 6B,C, which further confirmed the targeting potential of CPDs for brain tumor. We observed that CPDs could rapidly penetrate the BBB and reach the tumor site at 15 min after the injection, indicating that the intracerebral distribution of CPDs could be dynamically tracked due to the good tissue penetration capability of red fluorescence. The fluorescence intensity of CPDs in brain tumor reached the highest at 60 min and still remained strong even at 120 min, which was in good agreement with the in vitro BBB-penetration study of CPDs, demonstrating the high photostability and glioma targeting efficiency of CPDs. To further prove the targeting glioma by CPDs, tissue slices were prepared and detected by fluorescence microscopy. As shown in Figure S4, CPDs displayed higher distribution in glioma than that in the cerebral cortex and hippocampus of brain, suggesting that CPDs could target on brain glioma rather than normal brain tissues.

Generally, NPs could target a tumor due to the enhanced permeability and retention (EPR) effect.[60] However, the pore size of brain tumor vasculature is much smaller than that of peripheral tumors.[61] For example, Sarin et al. found that the up-limit pore size of brain tumor vasculature would be less than 20 nm,[62] whereas for extracranial tumors, the pore size was up to 1−5 μm.[63] In addition, NPs smaller than 5 nm were not suitable to serve as bioprobes for brain tumor imaging owing to their rapid excretion via renal filtration.[64] In this study, the diameter of CPDs is around 5.74 nm, which may contribute to the EPR effect and the prolonged circulation lifetime, leading to a high intratumoral accumulation.[35] Adsorptive-mediated transcytosis (AMT) is recognized as another important way of NPs crossing BBB.[16] AMT involves electrostatic interaction between the positive-charged NPs and the negative-charged endothelial cells. Therefore, the cationic CPDs could potentially facilitate their intratumoral delivery via AMT.[65] Overall, the combination of the upregulated BBB permeability, the EPR effect, the transcytosis via AMT, and the excellent tissue penetration ability of red fluorescence contributes to the high target to background signal ratio of CPDs to brain tumor.

Furthermore, CPDs could also clearly delineate the brain tumor boundary, demonstrating the feasibility of CPDs to surgically visualize and locate the brain tumor.[66] Veiseh et al. found that an iron oxide nanoprobe could visualize the brain tumor in vivo but the tumor tissue was precisely defined at 48 h after injection due to the slow BBB-penetration of the probe.[67] Therefore, our nanoprobe with rapid intratumoral distribution and bright red fluorescence emission in neoplastic tissues is highly desirable to the oncologist. Because of the high

DOI: 10.1021/acsomega.8b01169
ACS Omega 2018, 3, 7888−7896

tumor to normal tissue ratio of CPDs in the ex vivo fluorescence imaging studies, we infer that this nanoprobe holds the promise to provide real-time fluorescence imaging guidance during surgery to completely remove tumor tissues while minimizing the impairment of surrounding healthy neurological tissues.

3. CONCLUSIONS

In summary, CPDs possess long excitation/emission wavelengths, low toxicity, high photostability, and excellent biocompatibility. CPDs exhibit high internalization in glioma cells in time- and dose-dependent procedures, and internalized CPDs locate mainly in endolysosomal structures. In vitro and in vivo studies confirmed the BBB permeability of CPDs, contributing to the early stage diagnosis of brain disorders and the noninvasive visualization of the brain tumor without compromised BBB. In addition, CPDs could successfully distribute into the orthotopic brain glioma with high target to background signal ratio in vivo, demonstrating the feasibility to localize the brain tumor before surgery. Furthermore, owing to the high tumor to normal tissue ratio of CPDs under ex vivo conditions, our nanoprobe holds the promise to guide brain-tumor resection by real-time fluorescence imaging during surgery. Currently, on the basis of these desirable results, we are performing further research on the photothermal therapy effect of CPDs for malignant brain tumors.

4. EXPERIMENTAL SECTION

4.1. Materials. Dulbecco's modified Eagle's medium (DMEM) was purchased from HyClone. Fetal bovine serum (FBS) was purchased from Ausgenex (Australia). Penicillin−streptomycin and trypsin−ethylenediaminetetraacetic acid were obtained from Genview. DAPI, Hoechst 33342, LysoTracker Green DND-26, and MitoTracker Green were obtained from Thermo Fisher Scientific. Tetrazolium salt (MTT) and dimethyl sulfoxide (DMSO) were purchased from Sigma-Aldrich.

4.2. Synthesis of CPDs. CPDs were synthesized by one-step hydrothermal technology according to our previous work.[25] Briefly, 0.5 mmol *o*PD was dissolved in 10 mL of deionized water, 50 μL of HNO_3 (0.725 mmol) was added to it, and stirred well. The solution was then transferred to a poly(tetrafluoroethylene) Teflon-lined autoclave (25 mL) and heated at 200 °C for 10 h. Next, the reactor was cooled to room temperature. Finally, the CPDs solution was obtained through a 0.22 μm poly(ether sulfone) membrane and further dialyzed in a 500 Da dialysis bag.

4.3. Cell Culture. Human umbilical vein endothelial cells (HUVEC) and C6 cells were used in this study and obtained from the Chinese Academy of Sciences. The cells were cultivated in DMEM in a humidified incubator at 37 °C. The DMEM growth medium contained 10% FBS and 1% penicillin−streptomycin (10 000 U mL^{-1} penicillin and 10 000 μg mL^{-1} streptomycin).

4.4. Cytotoxicity. C6 glioma cells (1×10^4 cells per well) were seeded into a 96-well plate and incubated at 37 °C and 5% CO_2 for 24 h. After that, the medium was replaced by CPDs at a series of concentrations ranging from 50 to 400 μg mL^{-1} and the incubation was then continued for another 24 h. Subsequently, the medium containing the CPDs in each well was removed and replaced with 180 μL of serum-free medium and 20 μL of MTT solution (5 mg mL^{-1}). After further incubation for 4 h at 37 °C, the culture medium containing MTT in each well was replaced with 200 μL of DMSO to dissolve the formazan crystals, followed by shaking for 10 min. Finally, the absorbance of all wells was measured at 490 nm using a microplate reader (BioTek). The cell viability was obtained through the use of an absorbance percentage relative to the CPD-untreated cells.

4.5. Physiological Stability of CPDs. C6 cells were seeded into six-well culture plates (1×10^5 cells per well), incubated overnight, and then treated with CPDs (200 μg mL^{-1}) for another 2 h incubation. After that, the medium containing CPDs was filtrated and the ζ-potential of the filtrate solution was measured using a Zetasizer Nano ZS (Malvern Instruments). Meanwhile, the cells were washed, trypsinized, harvested, and centrifuged and then the collected samples were fixed with 2% glutaraldehyde at 4 °C overnight. This was followed by postfixation with 1% osmium tetroxide, dehydration, and infiltration. Then, the samples were embedded in Epon resin and thin-sectioned with 70 nm using a RMC PowerTome-XL ultramicrotome. Finally, the prepared sections were observed with a JEM-2200FS transmission electron microscope (JEOL, Japan).

4.6. Cellular Uptake of CPDs. C6 cells were seeded in 35 mm cell culture dishes at a density of 4×10^4 cells per dish and incubated overnight at 37 °C for CLSM imaging. To investigate the influence of incubation time, CPDs with a concentration of 200 μg mL^{-1} were incubated with C6 cells for a series of time periods (5, 30, 60, and 120 min). Then, the cells were rinsed three times and imaged using an Olympus IX81 confocal laser scanning microscope (Japan) with excitation/emission wavelengths at 559/570−670 nm. The similar procedures were performed to reveal the cellular uptake of CPDs in HUVEC for different time periods (5, 30, and 60 min). To identify the dose-dependent uptake kinetics of CPDs, CPDs with various concentrations (50, 100, 150, and 200 μg mL^{-1}) were incubated with the C6 cells for 1 h. The fluorescence intensity of cells was then detected using CLSM.

4.7. Subcellular Location of CPDs. C6 cells were seeded in dishes and incubated overnight as described above. We used organelle-specific probes, including LysoTracker Green DND-26 and MitoTracker Green to determine intracellular distribution of CPDs by detecting the colocalization of CPDs with lysosomes and mitochondria, respectively. CPDs with a concentration of 200 μg mL^{-1} were incubated with the cells for 5 min. LysoTracker Green DND-26 (75 nM) was then co-incubated with the cells for 85 min. Subsequently, the cells were incubated with Hoechst 33342 (0.6 μg mL^{-1}), which served as the blue fluorescence dye to locate the nucleus. After another 5 min incubation time, the cells were rinsed three times and examined using CLSM.

To investigate the colocalization of CPDs with mitochondria, CPDs (200 μg mL^{-1}) were incubated with the cells for 30 min. The cells were then co-incubated with MitoTracker Green (33 nM) for 15 min, followed by the incubation with Hoechst 33342 (0.6 μg mL^{-1}) for another 5 min. Finally, the cells were rinsed and imaged using CLSM. For CLSM imaging, excitation/emission wavelengths of Hoechst 33342, LysoTracker Green DND-26, MitoTracker Green, and CPDs were 405/425−475, 488/500−545, 488/500−545, and 559/575−675 nm, respectively.

4.8. BBB-Penetration Ability of CPDs in Vitro. Human umbilical vein endothelial cells (HUVEC) and C6 brain glioma cells were used to establish an in vitro BBB model according to

DOI: 10.1021/acsomega.8b01169
ACS Omega 2018, 3, 7888−7896

the previous studies.[68] First, the polycarbonate membranes of 12-well transwell plates (Corning Incorporated) were coated with rat-tail type I collagen before use. The 12-well plates were seeded with 1.5 mL of C6 cells at a density of 1×10^6 cells per well. When the C6 cells had successfully attached to the well surface, HUVEC at a density of 2×10^5 cells mL^{-1} (0.5 mL) were seeded into the transwell inserts and incubated to construct an in vitro BBB model through no-contact coculture. Subsequently, we evaluated the function of the BBB model through measuring the transendothelial electrical resistance (TEER) every day using a Millicell-ERS (Millipore). The following experiments were conducted on the fifth day when TEER reached more than 200 Ω cm^2. Previous studies had proved that the in vitro BBB model could produce reasonable permeability outcomes when TEER was >150 Ω cm^2.[69]

The CPDs at a concentration of 2 mg mL^{-1} in Hank's balanced salt solution (HBSS) was investigated with the in vitro BBB model. Before that, an MTT assay was used to evaluate the cytotoxicity of CPDs (2 mg mL^{-1}) after 2 h incubation with HUVEC and C6 cells. CPDs (2 mg mL^{-1}) were added into the transwell lumen of BBB model culture. After predetermined incubation intervals (30, 60, 90, and 120 min), the fluid in the lower compartment containing the CPDs, which had penetrated the biomimetic BBB in vitro, was withdrawn and moved into a 96-well plate for detecting the fluorescence signal at 590/20 nm excitation and 645/40 nm emission wavelengths using a microplate reader (BioTek). The percentage of CPDs that crossed the BBB was calculated on the basis of the fluorescence intensity of the fluid in the lower compartment.

4.9. BBB-Penetration Ability of CPDs in Vivo. Healthy male Sprague-Dawley rats were chosen to serve as an in vivo BBB model to assess the BBB-penetration ability of CPDs. First, CPDs in PBS solution (30 mg kg^{-1}, 200 μL) were injected into the rats through the tail vein. After different time periods (1 and 24 h), the rats were anesthetized by intraperitoneal injection with 10% of chloral hydrate (300 mg kg^{-1}). After that, the transcardiac perfusion with saline was performed for these rats. Then, the brain tissue of rats was exposed and harvested. Finally, the fluorescence signal of brain tissue was measured by an in vivo imaging system (IVIS Spectrum, Caliper) at the suitable excitation (Ex)/emission (Em) wavelengths (Ex/Em: 570/640 nm).

4.10. In Vivo and ex Vivo Imaging of Orthotopic Glioma-Bearing Rats. The establishment of orthotopic glioma model was performed according to previous studies.[70] Briefly, male Wistar rats (200−210 g) were anesthetized with 10% of chloral hydrate and immobilized on a stereotaxic apparatus. A sagittal incision was adopted to expose the cranium. Then, a hole was drilled at a point located at 1 mm anterior to the coronal suture and 3 mm right-lateral to the sagittal suture. Subsequently, 10 μL of PBS containing 6×10^5 C6 glioma cells was slowly and gently injected into the target point of the brain. Tumor growth was determined by magnetic resonance imaging (MRI) with a 1.5T scanner (Siemens Avanto, Germany) 13 days later. The C6 glioma-bearing rats were administered with 50 mg kg^{-1} of CPDs through the tail vein injection at 15 days after implantation. At different time points after injection, the fluorescent distribution of the brain was detected using an in vivo optical imaging system (IVIS Spectrum, Caliper). After that, the rats were sacrificed and then their brain tissues were harvested and photographed by a camera. Finally, the ex vivo fluorescence imaging was performed for these brain tissues. After fixation with 4% paraformaldehyde, the brain tissues were further dehydrated using 30% sucrose. Then, consecutive frozen sections with 10 μm thickness were prepared and stained with 0.5 μg mL^{-1} of DAPI for 5 min. The fluorescence distribution of brain tissues was observed using an Olympus IX71 fluorescence microscopy (Japan).

4.11. Live Subjects. All animal experiments were performed according to the protocols approved by the Animal Care and Ethics Committee of Jilin University in China.

■ ASSOCIATED CONTENT

Supporting Information

The Supporting Information is available free of charge on the ACS Publications website at DOI: 10.1021/acsomega.8b01169.

TEM images of CPDs in C6 cells; CLSM images of HUVEC incubated with CPDs; real-time in vivo imaging of brain glioma; distribution of CPDs in brain glioma (PDF)

■ AUTHOR INFORMATION

Corresponding Authors

*E-mail: znan8910@163.com. Phone: 86-15514371219 (N.Z.).
*E-mail: byangchem@jlu.edu.cn. Phone: 86-431-85168478. Fax: 86-431-85193423 (B.Y.).
*E-mail: lulaijin@hotmail.com. Phone: 86-431-81875560. Fax: 86-431-84808391 (L.L.).

ORCID

Bai Yang: 0000-0002-3873-075X

Notes

The authors declare no competing financial interest.

■ ACKNOWLEDGMENTS

This study was supported by the National Natural Science Foundation of China (nos. 81371363, 51433003, and 21504029) and the Science & Technology Development Project of Jilin Province (no. 20140311083YY).

■ REFERENCES

(1) Wen, P. Y.; Kesari, S. Malignant Gliomas in Adults. *N. Engl. J. Med.* **2008**, *359*, 492−507.
(2) Sanai, N.; Polley, M. Y.; McDermott, M. W.; Parsa, A. T.; Berger, M. S. An Extent of Resection Threshold for Newly Diagnosed Glioblastomas. *J. Neurosurg.* **2011**, *115*, 3−8.
(3) Donahue, M. J.; Blakeley, J. O.; Zhou, J.; Pomper, M. G.; Laterra, J.; van Zijl, P. C. Evaluation of Human Brain Tumor Heterogeneity Using MRI with Multiple T1-based Signal Weighting Approaches. *Magn. Reson. Med.* **2008**, *59*, 336−344.
(4) Haque, R.; Contreras, R.; McNicoll, M. P.; Eckberg, E. C.; Petitti, D. B. Surgical Margins and Survival after Head and Neck Cancer Surgery. *BMC Ear, Nose Throat Disord.* **2006**, *6*, No. 2.
(5) Sanai, N.; Berger, M. S. Glioma Extent of Resection and Its Impact on Patient Outcome. *Neurosurgery* **2008**, *62*, 753−766.
(6) Zhou, J.; Tryggestad, E.; Wen, Z.; Lal, B.; Zhou, T.; Grossman, R.; Wang, S.; Yan, K.; Fu, D. X.; Ford, E.; Tyler, B.; Blakeley, J.; Laterra, J.; van Zijl, P. C. Differentiation between Glioma and Radiation Necrosis Using Molecular Magnetic Resonance Imaging of Endogenous Proteins and Peptides. *Nat. Med.* **2011**, *17*, 130−134.
(7) Toms, S. A.; Lin, W. C.; Weil, R. J.; Johnson, M. D.; Jansen, E. D.; Mahadevan-Jansen, A. Intraoperative Optical Spectroscopy

DOI: 10.1021/acsomega.8b01169
ACS Omega 2018, 3, 7888−7896

Identifies Infiltrating Glioma Margins with High Sensitivity. *Neurosurgery* **2005**, *57*, 382−391.
(8) Nair, L. V.; Nair, R. V.; Shenoy, S. J.; Thekkuveettil, A.; Jayasree, R. S. Blood Brain Barrier Permeable Gold Nanocluster for Targeted Brain Imaging and Therapy: An in vitro and in vivo Study. *J. Mater. Chem. B* **2017**, *5*, 8314−8321.
(9) Scott, J. N.; Brasher, P. M. A.; Sevick, R. J.; Rewcastle, N. B.; Forsyth, P. A. How Often Are Nonenhancing Supratentorial Gliomas Malignant? A Population Study. *Neurology* **2002**, *59*, 947−949.
(10) Dimou, S.; Battisti, R. A.; Hermens, D. F.; Lagopoulos, J. A Systematic Review of Functional Magnetic Resonance Imaging and Diffusion Tensor Imaging Modalities Used in Presurgical Planning of Brain Tumour Resection. *Neurosurg. Rev.* **2013**, *36*, 205−214.
(11) Kircher, M. F.; Zerda, A. D. L.; Jokerst, J. V.; Zavaleta, C. L.; Kempen, P. J.; Mittra, E.; Pitter, K.; Huang, R.; Campos, C.; Habte, F.; Sinclair, R.; Brennan, C. W.; Mellinghoff, I. K.; Holland, E. C.; Gambhir, S. S. A Brain Tumor Molecular Imaging Strategy Using a New Triple-Modality MRI-Photoacoustic-Raman Nanoparticle. *Nat. Med.* **2012**, *18*, 829−834.
(12) D'Amico, R. S.; Kennedy, B. C.; Bruce, J. N. Neurosurgical Oncology: Advances in Operative Technologies and Adjuncts. *J. Neuro-Oncol.* **2014**, *119*, 451−463.
(13) Senders, J. T.; Muskens, I. S.; Schnoor, R.; Karhade, A. V.; Cote, D. J.; Smith, T. R.; Broekman, M. L. Agents for Fluorescence-guided Glioma Surgery: a Systematic Review of Preclinical and Clinical Results. *Acta Neurochir.* **2017**, *159*, 151−167.
(14) Craig, S. E. L.; Wright, J.; Sloan, A. E.; Brady-Kalnay, S. M. Fluorescent Guided Surgical Resection of Glioma Using Targeted Molecular Imaging Agents: A Literature Review. *World Neurosurg.* **2016**, *90*, 154−163.
(15) Popescu, M. A.; Toms, S. A. In vivo Optical Imaging Using Quantum Dots for the Management of Brain Tumors. *Expert Rev. Mol. Diagn.* **2006**, *6*, 879−890.
(16) Gao, X.; Li, C. Nanoprobes Visualizing Gliomas by Crossing the Blood Brain Tumor Barrier. *Small* **2014**, *10*, 426−440.
(17) Janib, S. M.; Moses, A. S.; Mackay, J. A. Imaging and Drug Delivery Using Theranostic Nanoparticles. *Adv. Drug Delivery Rev.* **2010**, *62*, 1052−1063.
(18) Li, C.; Xia, J.; Wei, X.; Yan, H.; Si, Z.; Ju, S. pH-Activated Near-Infrared Fluorescence Nanoprobe Imaging Tumors by Sensing the Acidic Microenvironment. *Adv. Funct. Mater.* **2010**, *20*, 2222−2230.
(19) Zhang, T. T.; Li, W.; Meng, G.; Wang, P.; Liao, W. Strategies for Transporting Nanoparticles across the Blood-Brain Barrier. *Biomater. Sci.* **2016**, *4*, 219−229.
(20) Zhao, A.; Chen, Z.; Zhao, C.; Gao, N.; Ren, J.; Qu, X. Recent Advances in Bioapplications of C-dots. *Carbon* **2015**, *85*, 309−327.
(21) Zheng, X. T.; Ananthanarayanan, A.; Luo, K. Q.; Chen, P. Glowing Graphene Quantum Dots and Carbon Dots: Properties, Syntheses, and Biological Applications. *Small* **2015**, *11*, 1620−1636.
(22) Ding, H.; Yu, S. B.; Wei, J. S.; Xiong, H. M. Full-Color Light-Emitting Carbon Dots with a Surface-State-Controlled Luminescence Mechanism. *ACS Nano* **2016**, *10*, 484−491.
(23) Tao, H.; Yang, K.; Ma, Z.; Wan, J.; Zhang, Y.; Kang, Z.; Liu, Z. In Vivo NIR Fluorescence Imaging, Biodistribution, and Toxicology of Photoluminescent Carbon Dots Produced from Carbon Nanotubes and Graphite. *Small* **2012**, *8*, 281−290.
(24) Zhang, J.; Cheng, F.; Li, J.; Zhu, J. J.; Lu, Y. Fluorescent Nanoprobes for Sensing and Imaging of Metal Ions: Recent Advances and Future Perspectives. *Nano Today* **2016**, *11*, 309−329.
(25) Liu, J.; Li, D.; Zhang, K.; Yang, M.; Sun, H.; Yang, B. One-Step Hydrothermal Synthesis of Nitrogen-Doped Conjugated Carbonized Polymer Dots with 31% Efficient Red Emission for In Vivo Imaging. *Small* **2018**, *14*, No. 1703919.
(26) Zhou, N.; Zhu, S.; Maharjan, S.; Hao, Z.; Song, Y.; Zhao, X.; Jiang, Y.; Yang, B.; Lu, L. Elucidating the Endocytosis, Intracellular Trafficking, and Exocytosis of Carbon Dots in Neural Cells. *RSC Adv.* **2014**, *4*, 62086−62095.
(27) Lim, S. Y.; Shen, W.; Gao, Z. Carbon Quantum Dots and Their Applications. *Chem. Soc. Rev.* **2015**, *44*, 362−381.
(28) Namdari, P.; Negahdari, B.; Eatemadi, A. Synthesis, Properties, and Biomedical Applications of Carbon-based Quantum Dots: An Updated Review. *Biomed. Pharmacother.* **2017**, *87*, 209−222.
(29) Zhang, J.; Hao, G.; Yao, C.; Hu, S.; Hu, C.; Zhang, B. Paramagnetic Albumin Decorated $CuInS_2$/ZnS QDs for $CD133^+$ Glioma Bimodal MR/Fluorescence Targeted Imaging. *J. Mater. Chem. B* **2016**, *4*, 4110−4118.
(30) Ducray, A. D.; Stojiljkovic, A.; Möller, A.; Stoffel, M. H.; Widmer, H. R.; Frenz, M.; Mevissen, M. Uptake of Silica Nanoparticles in the Brain and Effects on Neuronal Differentiation Using Different In Vitro Models. *Nanomedicine* **2017**, *13*, 1195−1204.
(31) Qian, M.; Du, Y.; Wang, S.; Li, C.; Jiang, H.; Shi, W.; Chen, J.; Wang, Y.; Wagner, E.; Huang, R. Highly Crystalline Multicolor Carbon Nanodots for Dual-Modal Imaging-Guided Photothermal Therapy of Glioma. *ACS Appl. Mater. Interfaces* **2018**, *10*, 4031−4040.
(32) Qiao, C.; Yang, J.; Chen, L.; Weng, J.; Zhang, X. Intracellular Accumulation and Immunological Responses of Lipid Modified Magnetic Iron Nanoparticles in Mouse Antigen Processing Cells. *Biomater. Sci.* **2017**, *5*, 1603−1611.
(33) Fakhoury, I.; Saad, W.; Bouhadir, K. H.; Nygren, P.; Schhneider-stock, R.; Gali-Muhtasib, H. Uptake, Delivery, and Anticancer Activity of Thymoquinone Nanoparticles in Breast Cancer Cells. *J. Nanopart. Res.* **2016**, *18*, No. 210.
(34) Zhao, F.; Zhao, Y.; Liu, Y.; Chang, X.; Chen, C.; Zhao, Y. Cellular Uptake, Intracellular Trafficking, and Cytotoxicity of Nanomaterials. *Small* **2011**, *7*, 1322−1337.
(35) Ruan, S.; Qian, J.; Shen, S.; Zhu, J.; Jiang, X.; He, Q.; Gao, H. A Simple One-Step Method to Prepare Fluorescent Carbon Dots and Their Potential Application in Non-invasive Glioma Imaging. *Nanoscale* **2014**, *6*, 10040−10047.
(36) Murali, K.; Kenesei, K.; Li, Y.; Demeter, K.; Környei, Z.; Madarász, E. Uptake and Bio-reactivity of Polystyrene Nanoparticles Is Affected by Surface Modifications, Ageing and LPS Adsorption: In Vitro Studies on Neural Tissue Cells. *Nanoscale* **2015**, *7*, 4199−4210.
(37) Zhang, S.; Gao, H.; Bao, G. Physical Principles of Nanoparticle Cellular Endocytosis. *ACS Nano* **2015**, *9*, 8655−8671.
(38) Maurer, L. L.; Yang, X.; Schindler, A. J.; Taggart, R. K.; Jiang, C.; Hsu-Kim, H.; Sherwood, D. R.; Meyer, J. N. Intracellular Trafficking Pathways in Silver Nanoparticle Uptake and Toxicity in *Caenorhabditis elegans*. *Nanotoxicology* **2016**, *10*, 831−835.
(39) Dash, B. C.; Réthoré, G.; Monaghan, M.; Fitzgerald, K.; Gallagher, W.; Pandit, A. The Influence of Size and Charge of Chitosan/Polyglutamic Acid Hollow Spheres on Cellular Internalization, Viability and Blood Compatibility. *Biomaterials* **2010**, *31*, 8188−8197.
(40) Tu, Z.; Achazi, K.; Schulz, A.; Mülhaupt, R.; Thierbach, S.; Rühl, E.; Adeli, M.; Haag, R. Combination of Surface Charge and Size Controls the Cellular Uptake of Functionalized Graphene Sheets. *Adv. Funct. Mater.* **2017**, *27*, No. 1701837.
(41) Zhang, L. W.; Monteiro-Riviere, N. A. Mechanisms of Quantum Dot Nanoparticle Cellular Uptake. *Toxicol. Sci.* **2009**, *110*, 138−155.
(42) Duncan, R.; Richardson, S. C. W. Endocytosis and Intracellular Trafficking as Gateways for Nanomedicine Delivery: Opportunities and Challenges. *Mol. Pharm.* **2012**, *9*, 2380−2402.
(43) Tang, B.; Fang, G.; Gao, Y.; Liu, Y.; Liu, J.; Zou, M.; Wang, L.; Cheng, G. Lipid-Albumin Nanoassemblies Co-loaded with Borneol and Paclitaxel for Intracellular Drug Delivery to C6 Glioma Cells with P-gp Inhibition and Its Tumor Targeting. *Asian J. Pharm. Sci.* **2015**, *10*, 363−371.
(44) Maurer, L. L.; Meyer, J. N. A Systematic Review of Evidence for Silver Nanoparticle-induced Mitochondrial Toxicity. *Environ. Sci.: Nano* **2016**, *3*, 311−322.
(45) Abbott, N. J. Astrocyte-endothelial Interactions and Blood-Brain Barrier Permeability. *J. Anat.* **2002**, *200*, 629−638.
(46) Ma, S. H.; Lepak, L. A.; Hussain, R. J.; Shain, W.; Shuler, M. L. An Endothelial and Astrocyte Co-culture Model of the Blood-Brain Barrier Utilizing an Ultra-thin, Nanofabricated Silicon Nitride Membrane. *Lab Chip* **2005**, *5*, 74−85.

DOI: 10.1021/acsomega.8b01169
ACS Omega 2018, 3, 7888−7896

(47) Xu, L.; Dan, M.; Shao, A.; Cheng, X.; Zhang, C.; Yokel, R. A.; Takemura, T.; Hanagata, N.; Niwa, M.; Watanabe, D. Silver Nanoparticles Induce Tight Junction Disruption and Astrocyte Neurotoxicity in a Rat Blood-Brain Barrier Primary Triple Coculture Model. *Int. J. Nanomed.* **2015**, *10*, 6105−6119.
(48) Lu, S.; Guo, S.; Xu, P.; Li, X.; Zhao, Y.; Gu, W.; Xue, M. Hydrothermal Synthesis of Nitrogen-doped Carbon Dots with Real-time Live-cell Imaging and Blood-Brain Barrier Penetration Capabilities. *Int. J. Nanomed.* **2016**, *11*, 6325−6336.
(49) Saraiva, C.; Praça, C.; Ferreira, R.; Santos, T.; Ferreira, L.; Bernardino, L. Nanoparticle-mediated Brain Drug Delivery: Overcoming Blood-Brain Barrier to Treat Neurodegenerative Diseases. *J. Controlled Release* **2016**, *235*, 34−47.
(50) Banks, W. A. From Blood-Brain Barrier to Blood-Brain Interface: New Opportunities for CNS Drug Delivery. *Nat. Rev. Drug Discovery* **2016**, *15*, 275−292.
(51) Hubbs, A. F.; Sargent, L. M.; Porter, D. W.; Sager, T. M.; Chen, B. T.; Frazer, D. G.; Castranova, V.; Sriram, K.; Nurkiewicz, T. R.; Reynolds, S. H.; Battelli, L. A.; Schwegler-Berry, D.; McKinney, W.; Fluharty, K. L.; Mercer, R. R. Nanotechnology: Toxicologic Pathology. *Toxicol. Pathol.* **2013**, *41*, 395−409.
(52) Domínguez, A.; Suárez-Merino, B.; Goñi-de-Cerio, F. Nanoparticles and Blood-Brain Barrier: The Key to Central Nervous System Disease. *J. Nanosci. Nanotechnol.* **2014**, *14*, 766−779.
(53) Georgieva, J. V.; Kalicharan, D.; Couraud, P. O.; Romero, I. A.; Weksler, B.; Hoekstra, D.; Zuhorn, I. S. Surface Characteristics of Nanoparticles Determine Their Intracellular Fate in and Processing by Human Blood-Brain Barrier Endothelial Cells In Vitro. *Mol. Ther.* **2011**, *19*, 318−325.
(54) Li, X.; Tsibouklis, J.; Weng, T.; Zhang, B.; Yin, G.; Feng, G.; Cui, Y.; Savina, I. N.; Mikhalovska, L. I.; Sandeman, S. R.; Howel, C. A.; Mikhalovsky, S. V. Nano Carriers for Drug Transport across the Blood Brain Barrier. *J. Drug Targeting* **2017**, *25*, 17−28.
(55) Ljubimova, J. Y.; Sun, T.; Mashouf, L.; Ljubimov, A. V.; Israel, L. L.; Ljubimov, V. A.; Falahatian, V.; Holler, E. Covalent Nanodelivery Systems for Selective Imaging and Treatment of Brain Tumors. *Adv. Drug Delivery Rev.* **2017**, *113*, 177−200.
(56) Yoon, H. J.; Lee, E. S.; Kang, M.; Jeong, Y.; Park, J. H. In Vivo Multi-photon Luminescence Imaging of Cerebral Vasculature and Blood-Brain Barrier Integrity Using Gold Nanoparticles. *J. Mater. Chem. B* **2015**, *3*, 2935−2938.
(57) Liu, D.; Lin, B.; Shao, W.; Zhu, Z.; Ji, T.; Yang, C. In Vitro and in Vivo Studies on the Transport of PEGylated Silica Nanoparticles across the Blood-Brain Barrier. *ACS Appl. Mater. Interfaces* **2014**, *6*, 2131−2136.
(58) Noh, G.; Youn, Y. S.; Lee, E. S. Preparation of Iron Oxide Nanoparticles Functionalized with Y-shaped Ligands for Brain Tumor Targeting. *J. Mater. Chem. B* **2016**, *4*, 6074−6080.
(59) Yan, H.; Wang, L.; Wang, J.; Weng, X.; Lei, H.; Wang, X.; Jiang, L.; Zhu, J.; Lu, W.; Wei, X.; Li, C. Two-Order Targeted Brain Tumor Imaging by Using an Optical/Paramagnetic Nanoprobe across the Blood Brain Barrier. *ACS Nano* **2012**, *6*, 410−420.
(60) Prabhakar, U.; Maeda, H.; Jain, R. K.; Sevick-Muraca, E. M.; Zamboni, W.; Farokhzad, O. C.; Barry, S. T.; Gabizon, A.; Grodzinski, P.; Blakey, D. C. Challenges and Key Considerations of the Enhanced Permeability and Retention Effect for Nanomedicine Drug Delivery in Oncology. *Cancer Res.* **2013**, *73*, 2412−2417.
(61) Gao, H.; Pang, Z.; Jiang, X. Targeted Delivery of Nanotherapeutics for Major Disorders of the Central Nervous System. *Pharm. Res.* **2013**, *30*, 2485−2498.
(62) Sarin, H.; Kanevsky, A. S.; Wu, H.; Brimacombe, K. R.; Fung, S. H.; Sousa, A. A.; Auh, S.; Wilson, C. M.; Sharma, K.; Aronova, M. A.; Leapman, R. D.; Griffiths, G. L.; Hall, M. D. Effective Transvascular Delivery of Nanoparticles across the Blood-Brain Tumor Barrier into Malignant Glioma Cells. *J. Transl. Med.* **2008**, *6*, 80.
(63) Carmeliet, P.; Jain, R. K. Angiogenesis in Cancer and Other Diseases. *Nature* **2000**, *407*, 249−257.
(64) Choi, H. S.; Liu, W.; Misra, P.; Tanaka, E.; Zimmer, J. P.; Ipe, B. I.; Bawendi, M. G.; Frangioni, J. V. Renal Clearance of Quantum Dots. *Nat. Biotechnol.* **2007**, *25*, 1165−1170.
(65) Li, C.; Wildes, F.; Paul Winnard, J.; Artemov, D.; Penet, M. F.; Bhujwalla, Z. M. Conjugation of Poly-L-lysine to Bacterial Cytosine Deaminase Improves the Efficacy of Enzyme/Prodrug Cancer Therapy. *J. Med. Chem.* **2008**, *51*, 3572−3582.
(66) Gao, X.; Yue, Q.; Liu, Z.; Ke, M.; Zhou, X.; Li, S.; Zhang, J.; Zhang, R.; Chen, L.; Mao, Y.; Li, C. Guiding Brain-Tumor Surgery via Blood-Brain-Barrier-Permeable Gold Nanoprobes with Acid-Triggered MRI/SERRS Signals. *Adv. Mater.* **2017**, *29*, No. 1603917.
(67) Veiseh, O.; Sun, C.; Fang, C.; Bhattarai, N.; Gunn, J.; Kievit, F.; Du, K.; Pullar, B.; Lee, D.; Ellenbogen, R. G.; Olson, J.; Zhang, M. Specific Targeting of Brain Tumors with an Optical/Magnetic Resonance Imaging Nanoprobe across the Blood-Brain Barrier. *Cancer Res.* **2009**, *69*, 6200−6207.
(68) Kuchler-Bopp, S.; Delaunoy, J. P.; Artault, J. C.; Zaepfel, M.; Dietrich, J. B. Astrocytes Induce Several Blood-Brain Barrier Properties in Non-neural Endothelial Cells. *NeuroReport* **1999**, *10*, 1347−1353.
(69) Reichel, A.; Begley, D. J.; Abbott, N. J. An Overview of In Vitro Techniques for Blood-Brain Barrier Studies. *Methods Mol. Med.* **2003**, *89*, 307−324.
(70) Gao, J. Q.; Lv, Q.; Li, L. M.; Tang, X. J.; Li, F. Z.; Hu, Y. L.; Han, M. Glioma Targeting and Blood-Brain Barrier Penetration by Dual-targeting Doxorubincin Liposomes. *Biomaterials* **2013**, *34*, 5628−5639.

DOI: 10.1021/acsomega.8b01169
ACS Omega 2018, 3, 7888−7896